Enhanced heat flux and flow structures in turbulent Rayleigh-Bénard convection with rough boundaries

Krishan Chand and Arnab Kr. De[*]

Department of Mechanical Engineering, Indian Institute of Technology Guwahati, Assam 781039, India

Pankaj Kumar Mishra

Department of Physics, Indian Institute of Technology Guwahati, Assam 781039, India

We numerically investigate the effect of rough boundaries on heat flux enhancement and flow structures in turbulent Rayleigh-Bénard convection of air (Pr = 0.7) confined in a two-dimensional cell of aspect ratio 2 for the Rayleigh number Ra in the range $10^6 \leqslant$ Ra $\leqslant 4.64 \times 10^9$. We consider three levels of roughness having maximum height as 5%, 10%, and 20% of the cell height. The presence of rough surfaces induces a significant enhancement in heat flux beyond a critical Rayleigh number Ra_c, the value of which strongly depends on the roughness height. The probability density function of the temperature fluctuations exhibits a bi-Gaussian distribution below Ra_c, while it displays exponential nature in the enhanced heat flux regime. The distinct nature of large-scale flow patterns is observed in this regime. While a stable double-roll state persists for the smallest roughness setup, the effect of corner rolls emerges in the intermediate level. The breakdown of the stable double-roll structure into multiple rolls is seen to be linked to higher heat flux owing to the efficient washing out effect in the roughness grooves. While a stronger horizontal motion elevates the shear production for the smallest roughness case, direct injection of plumes into the bulk improves the buoyancy production, leading to larger heat flux for the tallest roughness. Roughness heights are seen not to have any discernible effect on the overall flow strength. A vertical distribution of mean temperature indicates the presence of multilayer characteristics with the roughness-invariant near-wall region identified by a weakly nonlinear profile. The variation of the mean temperature in the intermediate layer plays a crucial role in heat transfer enhancement as it reflects the quality of ventilation of the entrapped fluid.

I. INTRODUCTION

Rayleigh-Bénard convection (RBC), a buoyancy-driven instability, in which a thin layer of the fluid is heated from below and cooled from the top, has been the prototypal system to study many complex flows observed in nature and engineering flow [1,2]. For a convection cell of fixed aspect ratio, flow inside it is governed by the two control parameters, namely, the Rayleigh number Ra $= g\beta \Delta T H^3 / \nu \alpha$ and the Prandtl number Pr $= \nu / \alpha$, where g is the acceleration due to gravity, ΔT is the temperature difference between the two horizontal plates separated by a distance H, and ν, β, and α are the kinematic viscosity, thermal expansion coefficient, and thermal diffusivity of the fluid, respectively.

---

[*]akd@iitg.ac.in

Over the past few decades, in RBC an intriguing question that has drawn immense attention from the scientific community is how the heat transport depends on the control parameters, in particular, on Ra in several regimes of turbulent flow [3,4]. This dependence is well established as Nu $\sim$ Ra^m, where the nondimensionalized heat flux is represented as the Nusselt number Nu and m is the scaling exponent. A number of theories of the heat transfer mechanism for a smooth convection cell have become popular over the years, such as the classical 1/3 scaling by Malkus [5], the ultimate regime in turbulent convection [6], and the boundary layer–bulk unified theory of Grossmann and Lohse [7–9]. It has been noticed that the transport mechanism in RBC could be significantly enhanced by introducing rough surfaces in the convection cell [10]. Practically, all the surfaces underneath the flows are rough with a variety of roughness topology, height, and distribution. Owing to a number of factors, such as an increase in wetted area, inherent forcing of boundary layer instability, and a greater trigger of plumes in the near-wall region, RBC over the rough surface has recently gained momentum as a leading research problem. In this paper we present a detailed numerical investigation of the enhanced heat flux mechanism induced by different mean heights of the random surfaces in the convection cell.

Several experimental and numerical investigations have indicated that rough isothermal surfaces influence the Nu(Ra) scaling exponent [11–13]. Shen et $al.$ [14] noticed an increment of 20% in the heat flux compared to those in the case of smooth surfaces when rough (V-shaped groove) top and bottom walls were used. On the basis of their data, they proposed that the boundary layer penetration controls the increment in heat flux. In a three-dimensional (3D) experiment, using random spherical roughness elements, Ciliberto and Laroche [15] obtained that the Nu(Ra) scaling exponent improves to 0.45 when the thermal boundary layer thickness lies between the tallest ($h = 1$ cm) and smallest ($h = 0.06$ cm) roughness elements. Advancing a similar type of ideas, Du and Tong [11] reported that Nu is enhanced by 76% and 41% in the taller ($h = 9$ mm) and shorter ($h = 3.2$ mm) roughness heights, respectively, due to the presence of strong secondary vortices inside the cavities. Later, using the experimental data for the roughness of nature such as triangular grooves, Roche et $al.$ [16] reported that the scaling exponents approach $m = 1/2$, which is a feature of the ultimate regime.

Using the sinusoidal roughness of the optimum wavelength ($\lambda_{opt} = 0.1$), Toppaladoddi et $al.$ [17] observed the enhanced exponent regime ($m = 0.483$) in the range $10^8 \leqslant$ Ra $\leqslant 3 \times 10^9$. The increased interaction between the boundary layer and the bulk region was attributed to the appearance of this enhanced scaling regime. In contrast, Zhu et $al.$ [18] showed that such a seemingly high exponent regime stays temporarily only from $10^8 \leqslant$ Ra $\leqslant 3 \times 10^9$ and for higher Ra reverts to the classical scaling ($m = 1/3$). Further, Zhang et $al.$ [19] obtained the critical height of roughness beyond which secondary vortices induce a better mixing in the valleys, thereby enhancing the heat flux. Most notably, by introducing the roughness of three different scales, Zhu et $al.$ [20] suggested that multiscale roughness extends the enhanced exponent regime up to three decades of Ra ranging from 10^8 to 10^{11}. This extension of the regime was attributed to the sustained plume-bulk interaction by the shorter roughness heights at higher Ra ($>3 \times 10^9$).

Recently, Dong et $al.$ [21] numerically investigated the effect of spatial arrangements for triangular roughness elements on heat flux (Nu) and Reynolds number (Re). Based on the arrangement, it was observed that the sparsely distributed roughness elements were responsible for lowering the threshold Rayleigh (Ra$_c$) number beyond which the heat flux suddenly starts increasing, whereas Ra$_c$ in a compact arrangement shifts to higher values. The compact models yielded higher heat flux than those obtained for the sparse cases where the reduced heat flux regime seems to be more prevalent due to the entrapment of more fluid inside the wider cavities formed. In terms of scaling laws, the sparse model yielded a higher Nu(Ra) scaling exponent with nearly the same Re(Ra) exponent, which indicated that the flow strength remains insensitive to the roughness arrangement.

Tummers and Steunebrink [10] proposed a different mechanism for the enhanced heat flux regime for the square roughness. They argued that as the large-scale circulation is responsible for carrying the thermal plumes from the boundary layer to bulk in a smooth cell, diffusion of thermal plumes is inevitable while traveling along the periphery. The square roughness used in the convection cell was found to break the large-scale circulation, which yielded a faster and
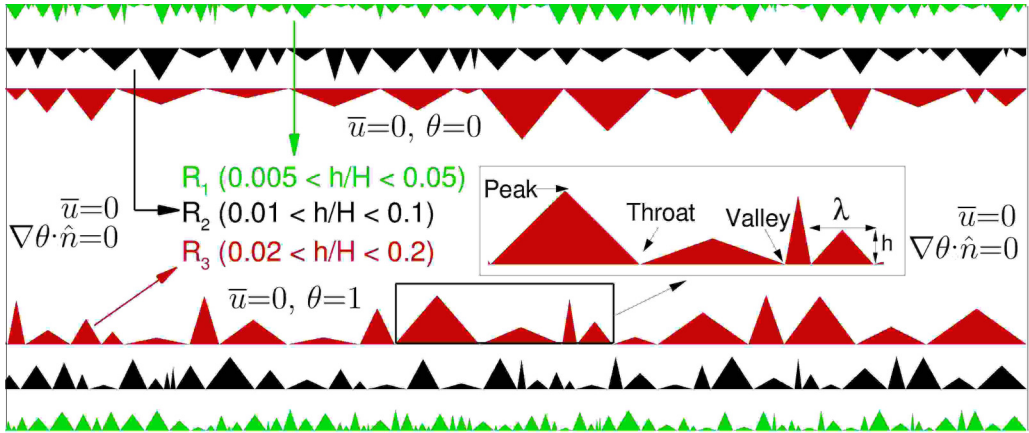
FIG. 1. Schematic diagram of three random roughness setups R_1, R_2, and R_3, which are characterized by their maximum heights. The inset shows a close-up view of the peak, valley, and throat regions associated with an element measured by its height h and base λ

direct interaction of hot (cold) plumes with the top (bottom) boundary layer. Thus, splashing of thermal plumes (both hot and cold) triggers instability in the boundary layer, resulting in emission of numerous thermal plumes to augment heat transfer. In addition, the fluid entrapped in the cavities creates more intense plumes with a longer lifetime. Such a phenomenon exists not only in a roughness-facilitated convection cell, but also in smooth cells, as reported by Chand *et al.* [22] at higher Ra in a 2D rectangular cell. The emission of such intense plumes was termed a thermal jet, but their insufficient intensity and the localized phenomenon resulted in a 2/7 power law. While varying the height of the ring-shaped obstacles and gap between them, Emran and Shishkina [23] observed that a taller height and wider gap are favorable for obtaining a higher heat flux, where cavities are fully washed out. However, the scaling exponent increases when cavities are partly washed out. Moreover, for very tall obstacles, large-scale circulation breaks down into smaller rolls that result in an increment of overall heat transfer [23].

Wang *et al.* [24] also reported a similar mechanism for enhanced heat flux. In a slender and rectangular tilted convective cell, they observed that a stable double-roll state reduces the heat flux, while an unstable triple-roll or single-roll state increases the heat flux owing to the enhanced mixing. These different roll structures were consequences of the inclination given to the cell. In their recent study [25], both the heat flux (Nu) and flow strength (Re) were found to depend upon the mean aspect ratio of the convection rolls, which was defined as the ratio of the aspect ratio and the number of large-scale rolls. Both global transport properties were observed to rise as the mean aspect ratio drops. In other words, for a fixed-aspect-ratio convection cell, a larger number of rolls results in higher Nu and Re. Thus, it shows that breaking of flow symmetry can lead to higher heat flux, which can be incited either using the roughness elements or by providing inclination to the convective cell.

So far, a single roughness scale (uniform height) has been used in almost all the studies on roughness-aided turbulent convection, where the flow interacts with the roughness elements nearly in the same manner. However, varying heights and wavelengths of the roughness elements may result in a different Nu(Ra) dependence and transport mechanism, as observed in [26]. Chand *et al.* investigated the role of near-wall dynamics in heat flux enhancement using different random roughness configurations [26]. It was observed that wider cavities strengthen the secondary vortices, which emit thermal plumes more frequently to enhance the heat flux. In RBC, note that, although small-scale structures play a crucial role in heat transport, the flow is primarily governed by large-scale rolls for relatively low Pr [27]. Using three different roughness heights marked as R_1, R_2, and R_3 (see Fig. 1), the present work is mainly focused on the role of large-scale rolls in the

heat transport mechanism associated with enhanced heat flux regimes. Moreover, by analyzing the global flow structures and production of turbulent kinetic energy near the rough surfaces, we find out how the so-called bulk-plume interaction improves in the roughness-aided configuration that is attributed to the augmented heat flux [17].

The regions near the rough elements and their geometric measure are shown schematically in Fig. 1, where boundary conditions are briefly mentioned. In the present work, we consider surfaces with triangular roughness elements that have random heights and appear without any order. Random numbers with normal distribution are generated which are assigned as the height h and base λ of the elements. In order to include a range of scales, the minimum height is taken as 10% of the maximum, which is nearly 0.05, 0.1, and 0.2 for R_1, R_2, and R_3, respectively. Since the measured total wetted area for the three cases is nearly the same, its effect is naturally eliminated. Totals of 152, 71, and 36 roughness elements are present in the R_1, R_2, and R_3 configurations, respectively. Note that the number of roughness elements becomes approximately doubled as the roughness configuration changes progressively from the smallest (R_1) to the tallest (R_3) heights. It is found that, despite nearly the same wetted area, the tallest roughness case yields maximum heat flux due to the presence of a multiple-roll state. On the other hand, a double-roll state (DRS) is observed to influence the heat flux the least.

The organization of the paper is as follows. Section II contains details of the mathematical formulations and numerical methods followed by the grid independence and verification of the numerical results with the earlier numerical studies performed using the rough boundaries. Section III presents the results on the enhanced heat flux scalings obtained for the three different random roughness heights followed by the analysis of flow structure and flow strength. Further, an extensive analysis of the characteristics of flow structure and its role in the enhanced heat transport in the vicinity of and far away from rough surfaces is given. The present work is concluded in Sec. IV.

II. NUMERICAL DETAILS

Using the Oberbeck-Boussinesq approximation, mass, momentum, and energy conservation equations for incompressible buoyancy-driven flows can be written in the nondimensional form as

$$\frac{\partial u_i}{\partial x_i} = 0, \tag{1}$$

$$\frac{\partial u_i}{\partial t} + \frac{\partial (u_i u_j)}{\partial x_j} = -\frac{\partial p}{\partial x_i} + \sqrt{\frac{\mathrm{Pr}}{\mathrm{Ra}}} \frac{\partial^2 u_i}{\partial x_j \partial x_j} + \theta \delta_{iy}, \tag{2}$$

$$\frac{\partial \theta}{\partial t} + \frac{\partial (u_j \theta)}{\partial x_j} = \frac{1}{\sqrt{\mathrm{Pr}\,\mathrm{Ra}}} \frac{\partial^2 \theta}{\partial x_j \partial x_j}, \tag{3}$$

where $x_i = (x, y)$ represents the Cartesian coordinates, p the pressure, $u_i = (u, v)$ the velocity field, $\theta = (T - T_C)/(T_H - T_C)$ the temperature, and δ_{ij} (=1 for $i = j$) the Kronecker delta. Note that the above equations are nondimensionalized using the temperature difference across the two plates $(T_H - T_C)$ as the temperature scale, the free-fall velocity $(\sqrt{g\beta \Delta T H})$ as the velocity scale, and the vertical spacing between the plates (H) as the spatial scale. The flow is simulated inside a two-dimensional rectangular box of aspect ratio $\Gamma = 2$ using air (Pr = 0.7) as the working fluid. Both rough surfaces are kept at a fixed temperature, while the adiabatic boundary condition is used along the lateral walls. A no-slip boundary condition is invoked for both the uneven surfaces and the lateral walls. We employ a standard random number generator with normal distribution to generate the amplitude h and wavelength λ of the individual roughness elements, as shown in Fig. 1. As h and λ are allowed to vary independently, a variety of triangular-shaped elements fill the horizontal plates. We have limited the base and height of the elements within 1–10 % of the maximum height and base. In order to create three different levels of roughness, the maximum height and base are chosen as 5%, 10%, and 20% of the cell height, which are referred to as the R_1, R_2, and R_3 configurations,
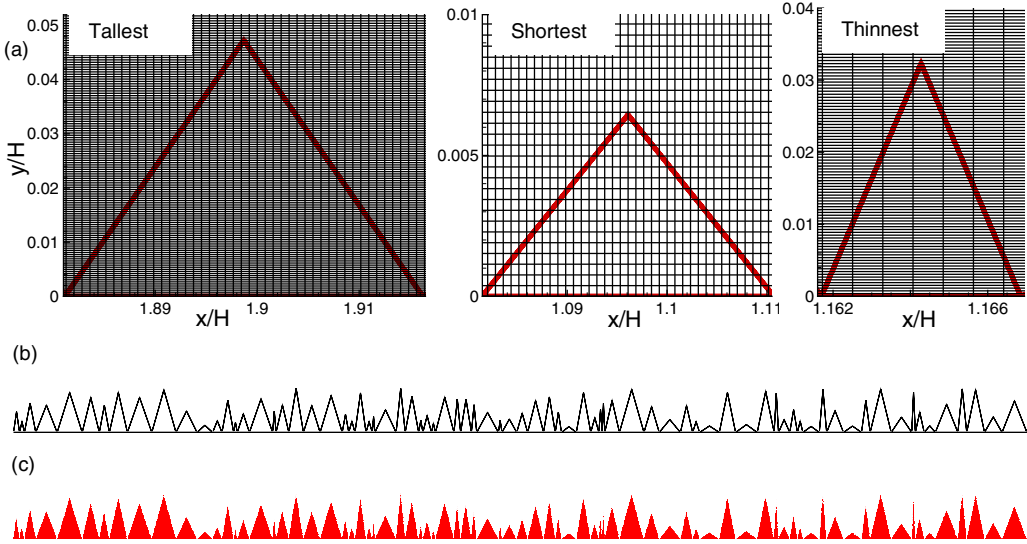
FIG. 2. (a) Three elements with extreme dimensions are shown with embedded mesh for the highest Ra ($=$ 4.64×10^9) and the smallest roughness case (R_1). (b) The linearized integral object (c) is identically reproduced by the zero-level set function

respectively (see Fig. 1). It should be noted that the range of a truly random distribution is likely to contain all possible heights and bases. However, since a finite axial length of the cell is used, only a finite number of such elements can be placed on the horizontal surfaces. Thus, in spite of choosing an element arbitrarily, a finite number of them limits the possibility of the (λ, h) combinations. The present setup is clearly an improved multiscale roughness which contains a number of scales for the height and base of the triangular roughness elements. Also note, by the virtue of such a choice, that the aspect ratio h/λ of the elements is also random, which does not have any predefined order.

In order to resolve the widely varying roughness elements, a sufficient number of cells are used inside them. Figure 2(a) shows three elements of extreme dimensions which are well resolved in the vertical direction. The numbers of cells inside the shortest and tallest elements are 13 and 71 for Ra $= 10^6$ and 17 and 118 for Ra $= 4.64 \times 10^9$, respectively. The excellent resolution is reflected in the volume rendering of the zero-level set function [28,29] in Fig. 2(c), which agrees identically with the exact linearized integral object sitting on the bottom plate [Fig. 2(b)]. The errors in volume thus reproduced are found to be 0.13% and 0.04% for the two extreme meshes.

A nonstaggered finite-volume technique integrated with a diffuse interface immersed boundary method [29] is used to solve the above set of equations (1)–(3). Before carrying out the simulations, we conduct a validation test by reproducing the results obtained by Zhu et $al.$ [18] and a grid-independence test for four different mesh sizes. Using sufficiently refined mesh stretched in the wall-normal direction and a time increment of 10^{-4}, we validate the present setup for sinusoidal roughness geometry of equal height ($h = 0.1$) and wavelength ($\lambda = 0.1$) at two Rayleigh numbers Ra $= 2.2 \times 10^8$ and 2.2×10^9. In terms of global heat transport, a maximum of 7% (average 3%) variation in Nu confirms the correctness of the present setup. Figure 3(a) shows a direct comparison of Nu as obtained in the present work and that reported by Zhu et $al.$ [18], which shows that the results computed using the present setup are in good agreement with the previous study. Moreover, we show a comparison of the mean vertical temperature profile averaged over the horizontal plane in Figs. 3(b) and 3(c). For the grid independence test, as shown in Fig. 4, we quantify the change in Nu and temperature variance σ_θ for four progressively refined meshes at Ra $= 4.64 \times 10^9$. These
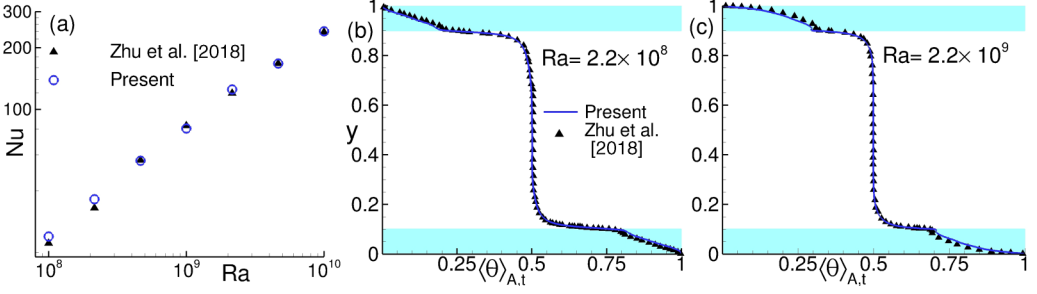
FIG. 3. (a) Nu comparison of the present work and Zhu *et al.* [18] for sinusoidal roughness geometry. Mean temperature profiles for (b) Ra $= 2.2 \times 10^8$ and (c) Ra $= 2.2 \times 10^9$ are compared with the previous data [18]. Note that geometric attributes of the roughness configuration (sinusoidal) remain the same for the comparison. The shaded region indicates the roughness area

changes are represented by ΔNu and $\Delta\sigma_\theta$, computed as

$$\Delta\text{Nu} = |\frac{\text{Nu}_i - \text{Nu}_{i-1}}{\text{Nu}_{i-1}}| \times 100, \quad (4)$$

$$\Delta\sigma_\theta = |\frac{\sigma_{\theta,i} - \sigma_{\theta,i-1}}{\sigma_{\theta,i-1}}| \times 100, \quad (5)$$

where $\sigma_\theta = \langle \theta'^2 \rangle_{V,t}$. Note that $\langle \cdots \rangle_{V,t}$ and the prime represent the volume-time average and fluctuation, respectively, and i (=1, 2, 3, 4) represents the mesh size in increasing order. Figures 4(a) and 4(b) clearly show that changes in both ΔNu and $\Delta\sigma_\theta$ become insignificant as we refine the mesh beyond M_3. Considering the diminishing return and significant increase in computational cost, mesh M_3, given by 2560×1620, is used for subsequent calculations.

Numerical details of all the simulated cases are listed in Table I. The nonuniform mesh in the wall-normal direction is refined close to the rough surfaces, whereas a uniform meshing is used in the horizontal direction. For adequate spatial resolution, the maximum grid spacing is kept smaller than the analytically estimated Kolmogorov length scale $[\eta = H \Pr^{1/2} (\text{Nu} - 1)^{-1/4} \text{Ra}^{-1/4}]$. It also satisfies the criterion of the minimum number of grid points inside the thermal boundary layer [30]. In particular, $\Delta y_{max}/\eta = 0.82$ and 2560×1620 grid points are used in the horizontal and vertical directions, respectively, for the most demanding case Ra $= 4.64 \times 10^9$. Statistical sampling
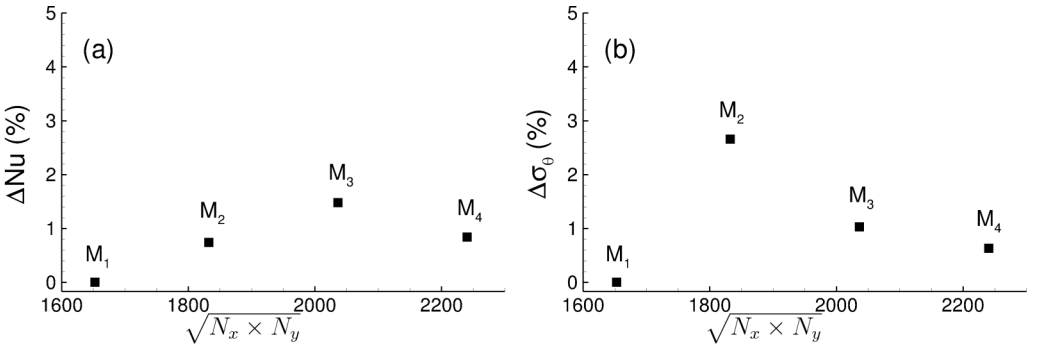

FIG. 4. Variation of change in volume-averaged (a) Nu and (b) temperature variance σ_θ for four progressively refined meshes (M_1, M_2, M_3, and M_4) represented as $\sqrt{N_x \times N_y}$ at Ra $= 4.64 \times 10^9$. Here N_x and N_y are the number of grid points in the x and y directions, respectively. Temperature variance is computed as $\sigma_\theta = \langle \theta'^2 \rangle_{V,t}$, where $\langle \cdots \rangle_{V,t}$ and the prime represents the volume-time average and fluctuation, respectively

TABLE I. Details of the simulation parameters for the three roughness configurations R_1, R_2, and R_3. From left to right, Ra is the Rayleigh number; N_x and N_y are the number of grid points in the x and y directions, respectively; N_{BL} is the number of grid points inside the thermal boundary layer calculated from the smooth case; Nu_{ref} is the reference Nusselt number taken from Zhu *et al.* [20] for multiscale roughness; and Nu_{comp} is the computed Nusselt number in the present work. Here an underline, parentheses, and an overline mark the onset of the enhanced heat flux regime in the R_1, R_2, and R_3 cases, respectively

Ra	$N_x \times N_y$ for R_i (i = 1, 2, 3)	N_{BL}	Nu_{ref} Zhu *et al.* [20]	Nu_{comp} R_1	R_2	R_3	Smooth
10^6	1000×600	87		6.84	6.06	5.08	07.35
2×10^6	1000×600	85			6.53	6.17	
3×10^6	1000×600	75		8.49	7.07	6.89	09.01
6×10^6	1000×600	74			8.48	10.11	
$\overline{10^7}$	1000×600	59		10.61	9.73	$\overline{12.00}$	12.44
3×10^7	1000×600	48		14.19	16.44	19.25	17.45
(5.50×10^7)	1000×600	42		16.70	(20.97)	24.87	20.98
10^8	1200×600	24	20.8	20.28	26.19	32.45	25.08
$\underline{2.15 \times 10^8}$	1200×700	19	30.1	$\underline{28.98}$	37.59	44.38	32.18
$\overline{4.64 \times 10^8}$	1400×800	16	43.6	44.34	53.69	61.81	40.93
10^9	2000×1000	13	63.1	64.05	76.02	86.67	51.50
2.15×10^9	2000×1400	13	92.2	88.88	105.60	117.48	60.49
4.64×10^9	2560×1620	11	130.3	132.72	145.73	158.29	74.92

is carried out for at least 200 free-fall time units once the flow attains a statistically steady state and $\langle \phi \rangle_V$, $\langle \phi \rangle_{V,t}$, and $\langle \phi \rangle_{A,t}$ denote the volume, volume-time, and area-time ensemble of a variable $\phi(\overline{x}, t)$, respectively. Note that, to determine Ra in roughness cases, the effective height of the convection cell is computed by considering the same volume of fluid as in the smooth case [20].

III. RESULTS AND DISCUSSION

In the following, we present our observation related to the enhancement of Nusselt number for different roughness heights, which have been denoted by R_1, R_2, and R_3.

A. Enhanced heat flux regime

Rough surfaces in thermal convection cells have a role to play in efficient heat transfer. The nondimensional heat flux (Nu) is computed using $Nu = \sqrt{Ra\,Pr}\langle v\theta \rangle_V - \langle \partial_z \theta \rangle_V$. Since Nu is perceived as the measure of heat transfer rate from the underlying surface and Ra contains the applied thermal forcing, the exponent in the $Nu \sim Ra^m$ scaling law acts as the key to heat transfer enhancement. Among a few others, roughened surfaces have been observed to push the classical Malkus [5] exponent of 1/3 towards what Kraichnan [6] foresaw as the ultimate regime in thermal convection characterized by the half scaling ($m = 1/2$). In what follows, we begin with the comparison of Nu for different roughness heights. Figure 5(a) shows Nu obtained for the multiscale roughness by Zhu *et al.* [20], the pyramid-shaped roughness by Xie and Xia [31], the three present random roughness configurations, and a smooth cell. Clearly, the R_3 random roughness shows higher Nu as compared to the other configurations. Note that the wetted area for the present cases differs from the references; however, based on the criterion of the same effective Ra, the above comparison is made. Interestingly, the triple-scale and the smallest roughness (R_1) used in the present work yield the same Nu beyond $Ra = 10^8$. Note that the triple-scale roughness in [20] was termed multiscale roughness. However, the presence of a range of roughness scales which have no preconceived order
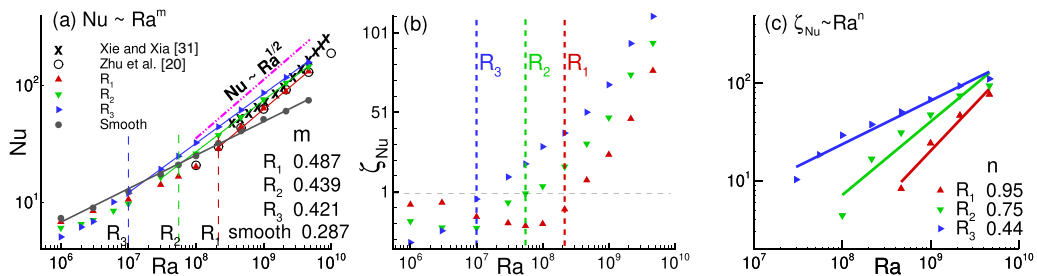
FIG. 5. (a) Comparison of Nu among the three roughness configurations and the previously reported data [20,31]. Vertical dashed lines represent the onset of enhanced heat flux regimes and m shows the Nu(Ra) scaling exponent. (b) Normalized heat flux ζ_{Nu} as a function of Ra, where vertical dashed lines again mark the onset of enhanced heat flux regimes. (c) Power-law fitting $\zeta_{Nu} \sim Ra^n$ in the enhanced heat flux regime suggests that smaller roughness promotes a greater rate of enhancement

in the present work makes it close to reality and also yields higher heat flux as compared to the previous roughness configurations.

A comparison of $Nu \sim Ra^m$ scaling with the smooth surface is in order. Figure 5(a) shows a least-squares fit of the data, resulting in three different exponents as $m = 0.487, 0.439$, and 0.421 for the R_1, R_2, and R_3 cases, respectively. Moreover, it also shows a different onset of the enhanced heat flux regime given by the critical Rayleigh number $Ra_c = 2.15 \times 10^8, 5.50 \times 10^7$, and 1×10^7 for R_1, R_2, and R_3, respectively. Since taller heights have a higher tendency to penetrate the boundary layers, lower values of Ra_c in R_2 and R_3 are expected [18]. The exponent in R_1 is close to that obtained by Toppaladoddi *et al.* [17] and Zhu *et al.* [20], which signifies the improved bulk-plume interaction by increasing the intense plume-emitting spots. On the other hand, breaking of large-scale rolls into smaller ones is responsible for the enhanced exponent in the R_2 and R_3 cases. Such a phenomenon was previously reported in the inclined convection cell. The random roughness used in the present work shows the same without any inclination.

Next, heat flux in the three roughness cases is compared. To exclude the effect of the wetted area in Nu, we keep it nearly the same in the three roughness cases. Figure 5(b) shows the variation of normalized heat flux, $\zeta_{Nu} = (Nu - Nu_0)/Nu_0$, as a function of Ra for the three roughness cases, where Nu_0 indicates the heat flux for the smooth case. In order to highlight the differences in Nu, the enhanced heat flux regime is further represented by $\zeta_{Nu} > 0$. In this regime, the tallest roughness (R_3) produces the maximum ζ_{Nu} and it drops with the configurations characterized by their maximum roughness height. In the enhanced heat flux regime ($\zeta_{Nu} > 0$), it is observed that the normalized heat flux obeys a power-law behavior as $\zeta_{Nu} \sim Ra^n$, where n is the scaling exponent. As shown in Fig. 5(c), a least-squares fit of the data yields $n = 0.95, 0.75$, and 0.44 for the R_1, R_2, and R_3 cases, respectively. Evidently, the exponent drops as the maximum roughness height increases. Surprisingly, the effect of roughness height is not limited to only increase in heat flux. The larger the maximum height of roughness, the greater the heat flux enhancement. However, the smaller the maximum height, the higher the rate of increase of ζ_{Nu} with Ra. This indicates a complex behavior of the surface roughness in heat transfer enhancement. The one with the highest gain does not extend for the entire spectrum of Ra, as smaller roughness yields a high rate of increase of Nu over Nu_0 at large Ra.

In the studied Ra range, we further investigate the probability density function (PDF) of temperature fluctuations θ' in the bulk region (center of the convection cell) to observe the effect of roughness there. The PDF is computed for at least 200 free-fall time units of sampling length. Figures 6(a)–(c) show the PDF of temperature fluctuations in the R_1, R_2, and R_3 cases, respectively. It should be noted that the transition in the distribution of temperature fluctuations has been used to demarcate different turbulent states [32]. In a recent study, Chand *et al.* [22] described the transition to a single-peak distribution as the sign of attainment of a highly turbulent state which modifies
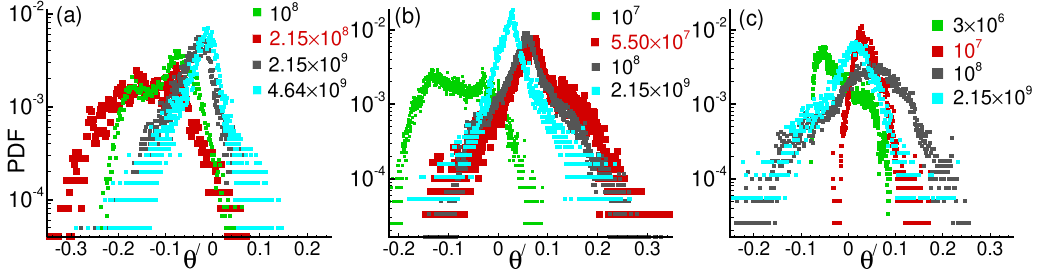
FIG. 6. PDF of temperature fluctuations (θ') in the bulk (center of the domain), showing the transition from two peaks (bi-Gaussian) to a single-peak (exponential) distribution in the (a) R_1, (b) R_2, and (c) R_3 configurations. The PDF at the critical Rayleigh number Ra_c in the three configurations is shown by the red color.

the temperature statistics. With increasing Ra, Castaing *et al.* [3] found that the PDF of θ' changes from a Gaussian to an exponential distribution, showing the transition to the hard-turbulent regime. Salort *et al.* [33] showed the change in histogram from Gaussian to a single-peak shape, when the probe was moved from the boundary layer region to the bulk. In the present study, a clear transition from two-peak behavior (bi-Gaussian distribution) to a single peak (exponential distribution) is evident in all three configurations at the critical Rayleigh numbers $(Ra_c) = 2.15 \times 10^8, 5.50 \times 10^7$, and 10^7, respectively, for R_1, R_2, and R_3. We note here that the distribution function is closer to a Gaussian only for the R_3 case beyond Ra_c. This transition confirms the attainment of the enhanced heat flux regime and also the modified Nu(Ra) scaling exponent. However, since such an onset occurs early (smaller Ra) for taller roughness, the distribution function having a single peak has a connection with a uniform flatter profile with significant scatter and longer tails. On the other hand, at small roughness, the onset occurs at a larger Ra when the distribution has become polarized with a sharp peak and virtually nonexistent tails. Thus, the onset of the enhanced heat flux regime occurs at relatively different flow states, which clearly indicates the role of the average height of the roughness elements, though they do not appear in any specific pattern.

It is generally assumed that in the ultimate regime the role of the boundary layer vanishes and the dissipation rate in the bulk dominates. In contrast to the smooth case, Zhu *et al.* [18] observed that the thermal dissipation rate increases with Ra inside the cavity region for monoscale roughness where the scaling regime reverts to the classical one. However, the dissipation rate was not evaluated for the multiscale roughness [20] where the 1/2 scaling was seen to be sustained. We show that the onset of the enhanced exponent regime can be linked to the thermal dissipation rate ϵ_θ calculated for the near-wall (NW) and bulk (BK) regions characterized by the maximum roughness heights ($h_{\max,b}$ and $h_{\max,t}$). In order to quantify them, we consider the definitions

$$\langle \epsilon_{\theta,NW} \rangle_{V,t} = \frac{1}{2} \left[\frac{1}{h_{\max,b}} \int_0^{h_{\max,b}} \langle \epsilon_\theta \rangle_{A,t}(y) dy + \frac{1}{h_{\max,t}} \int_{H-h_{\max,t}}^H \langle \epsilon_\theta \rangle_{A,t}(y) dy \right], \quad (6)$$

$$\langle \epsilon_{\theta,BK} \rangle_{V,t} = \frac{1}{H - (h_{\max,b} + h_{\max,t})} \int_{h_{\max,b}}^{H-h_{\max,t}} \langle \epsilon_\theta \rangle_{A,t}(y) dy. \quad (7)$$

As shown in Fig. 7, it is evident that a drop in $\epsilon_{\theta,NW}$ for rough cases is terminated at the point of onset of the enhanced heat flux regime and subsequently $\epsilon_{\theta,NW}$ becomes invariant to Ra. The saturation in dissipation rates in the near-wall region indicates the increased active spots that actively participate in thermal plume emission. These entrapped emitted thermal plumes form secondary flow structures in the near-wall regions. Hence, the dissipation rate associated with the locally entrapped structures balances the assumed drop in the dissipation rates, which otherwise contributes to the bulk region in the absence of entrapped flow structures in a smooth case. On the other hand, ϵ_θ continues to drop in the bulk region, though at a lesser rate. Here the dominance of the boundary
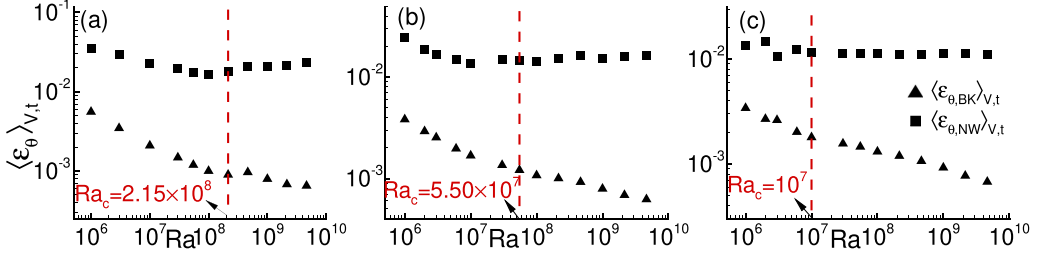
FIG. 7. Thermal energy dissipation rate ϵ_θ for the near-wall (squares) and bulk region (triangles) for the (a) R_1, (b) R_2, and (c) R_3 configurations. In the near-wall region, the dissipation rates indicate a visible discontinuity at the critical Ra, shown here by dashed lines, beyond which it becomes Ra invariant.

layer at high Ra arrests the otherwise monotonic drop in $\epsilon_{\theta,NW}$ while the bulk contribution continues to fall. The dominance of ϵ_θ in the near-wall region seems to indicate the importance of the boundary layer even in the enhanced heat flux regime in the present range of Ra, though Zhu *et al.* [18] observed otherwise at a higher thermal forcing in their monoscale roughness calculations.

Further, we study the dependence of global dissipation rates on Ra to ascertain the attainment of a higher Nu(Ra) scaling exponent in the enhanced heat flux regimes, as shown in Fig. 8. The global dissipation rates are estimated by considering the entire volume. Both ϵ_u and ϵ_θ can be written in terms of the global heat transport properties as

$$\langle \epsilon_u \rangle_{V,t} = \sqrt{\frac{\mathrm{Pr}}{\mathrm{Ra}}}(\mathrm{Nu}_{\epsilon_u} - 1), \quad \langle \epsilon_\theta \rangle_{V,t} = \frac{1}{\sqrt{\mathrm{PrRa}}}\mathrm{Nu}_{\epsilon_\theta}, \tag{8}$$

where the respective Nu are calculated based on the dissipation of kinetic ($\langle |\nabla u| \rangle_{V,t}$) and thermal energy ($\langle |\nabla \theta| \rangle_{V,t}$). Beyond the Ra_c, global dissipation rates become nearly invariant to Ra in all three roughness cases. With Nu $\sim \mathrm{Ra}^{1/2}$ scaling, as suggested by Eq. (8), ϵ becomes Ra invariant, which is clearly seen for Ra $> \mathrm{Ra}_c$. On the other hand, an interesting feature emerges before the transition (below Ra_c) to the enhanced heat flux regime. Here the dissipation rate drops with an exponent of $-3/14$, which can be theoretically obtained by assuming Nu $\sim \mathrm{Ra}^{2/7}$ in Eq. (8). Clearly, the best fit of the data reveals that R_1 nearly follows the 2/7 power law, while it deviates as the average roughness height increases. The prevailing 2/7 law in the R_1 case indicates the strong dominance of a double-roll state and an ineffective roughness-flow interaction. In other words, the rough surface, in this case, is inactive due to a weak thermal forcing and the fluid close to the asperities behave similarly to the smooth case.
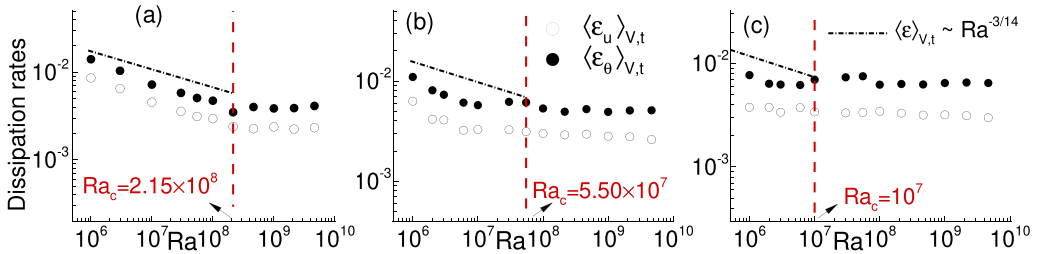

FIG. 8. Variation of the volume-averaged thermal (closed symbols) and kinetic (open symbols) energy dissipation rates with Ra in (a) R_1, (b) R_2, and (c) R_3 configurations. While the vertical dashed lines show the critical Ra_c beyond which the enhanced heat flux regime is obtained, the dash-dotted lines indicate $\epsilon \sim \mathrm{Ra}^{-3/14}$, which follows from the power law Nu $\sim \mathrm{Ra}^{2/7}$.

B. Flow structures in enhanced heat flux regime

In natural convection, thermal plumes play a crucial role in the heat transfer phenomenon [27]. These plumes are detached boundary layer structures responsible for the Nu(Ra) scaling law [3]. However, the heat transport mechanism in the rough configuration is different from those in the smooth case. In the latter, hot fluid gains sufficient energy to become unstable and rises from the boundary layers. In contrast, roughness elements help detach the hot fluid attached to them and thereby augment the heat transport properties. Note that the emission of thermal plumes and detachment are two different phenomena. Therefore, one way to influence the heat flux is by varying the plume-emission process and its morphology. On the other hand, altering the large-scale rolls, which drive these plumes, is another way to enhance the heat flux [24]. While the former is responsible for enhanced heat flux in the roughness case, the latter has been observed for the tilted cells [24]. Interestingly, in the present work, both have been observed to modify the scaling laws.

In an experimental study, Shen *et al.* [14] observed large-sized thermal plumes in the bulk region, which enhanced the heat flux. Later, Stringano *et al.* [34] found the edges of the roughness elements to be the most active plume-emission spots. By varying the geometric properties of roughness elements, Wagner and Shishkina [35] found that wider grooves interrupt the large-scale flow structures and strengthen the induced secondary vortices. These vortices wash out the cavities and weaken the boundary layer perturbation to make the transport process similar to that in the smooth case. In contrast, a lack of ventilation in the cavities results in intermittent interaction between large-scale rolls and the fluid resting in the cavities. This interaction sustains the perturbation of the boundary layers. Later, Toppaladoddi *et al.* [17] and Zhu *et al.* [20] attributed the enhanced heat flux and scaling exponent to the increased bulk-plume interaction. Since all of these investigations dealt with the uniform roughness, it is interesting to see how the process of plume emission and its interaction with the bulk respond to random roughness configurations.

Figure 9 shows the instantaneous temperature field for the three highest Ra cases, where Ra increases from top to bottom. In all three roughness cases, numerous small and bright structures appear with an increase in Ra due to rising plume-emitting spots (active peaks). It is observed that thermal plumes become finer with Ra and also change with roughness configuration. The size of the emitted thermal plumes changes from R_1 [Figs. 9(a), 9(d), and 9(g)] to R_3 [Figs. 9(c), 9(f), and 9(i)] due to geometrical changes in their nucleation site. In R_3, larger thermal structures are present, whereas they are thin and tiny in the R_1 case. In the smallest roughness case, a persistent two-roll structure appears for all three Ra cases. However, in the other two configurations, the highly random movement of thermal plumes appears due to multiple rolls, which is ascertained in the subsequent discussion.

To understand what triggers the enhanced global heat transport properties, we look into the time-averaged temperature field. Figure 10 shows the large-scale thermal structures overlaid by streamlines for the three roughness configurations. For R_3, the flow structures are shown for the entire simulated Ra, while for the other configurations (R_2 and R_1), only the smallest [Figs. 10(a), 10(g), and 10(j)], critical [Figs. 10(b), 10(h), and 10(k)], and highest [Figs. 10(c)–10(f), 10(i), and 10(l)] Ra cases are presented. Beginning with the tallest roughness [R_3 in Figs. 10(a)–10(f)], the double-roll state at a smaller Ra ($<10^7$) transforms into a triple-roll state at the critical $Ra_c = 10^7$. These rolls further break down into multiple rolls as Ra increases, as shown in Figs. 10(c)–10(f). Apparently, smaller rolls have a higher tendency to wash out the cavities than the bigger ones due to their ability to enter the narrow spaces between the roughness elements. The boundary layer under the influence of these strong rolls tends to leave the surface early, resulting in a frequent emission of arbitrarily shaped thermal plumes. Therefore, breaking of large-scale rolls into smaller ones explains how the so-called bulk-plume interaction increases in this configuration, which induces an early onset of enhanced heat flux regime and improves the Nu(Ra) exponent.

In contrast to R_3, where a transition from a double-roll state to a multiple-roll state is observed, two primary rolls persist for the entire simulated Ra regime for R_2. Nevertheless, the striking feature in this configuration is the contribution of corner rolls. At lower Ra ($<Ra_c$), weak corner rolls are

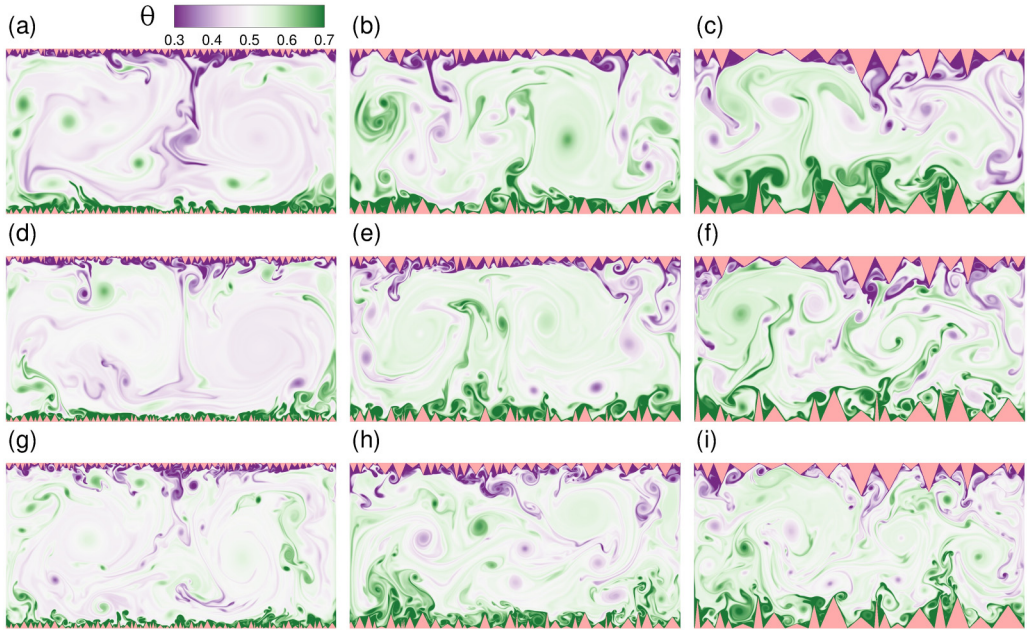FIG. 9. Instantaneous temperature field showing variation of flow structures in (a), (d), and (g) R_1, (b), (e), and (h) R_2, and (c), (f), and (i) R_3 cases at (a)–(c) Ra $= 10^9$, (d)–(f) Ra $= 2.15 \times 10^9$, and (g)–(i) Ra $= 4.64 \times 10^9$

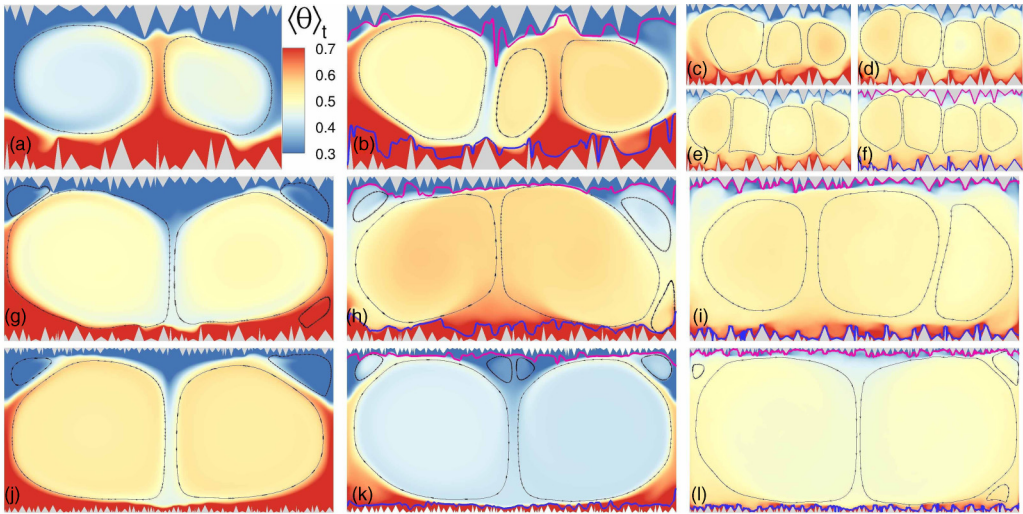FIG. 10. Time-averaged temperature field superimposed with streamlines for (a)–(f) R_3, (g)–(i) R_2, and (j)–(l) R_1 configurations. (b), (h), and (k) Critical Ra_c cases (10^7 for R_3, 5.50×10^7 for R_2, and 2.15×10^8 for R_1). Note that the (a), (g), and (j) represent Ra $= 10^6$, while (c)–(f), (i), and (l) indicate Ra $= 4.64 \times 10^9$. In addition, (a)–(f) indicate the transformation of large-scale rolls with Ra. The blue and pink lines show the thermal boundary layer at the bottom and top surfaces to reveal their influence on large-scale rolls
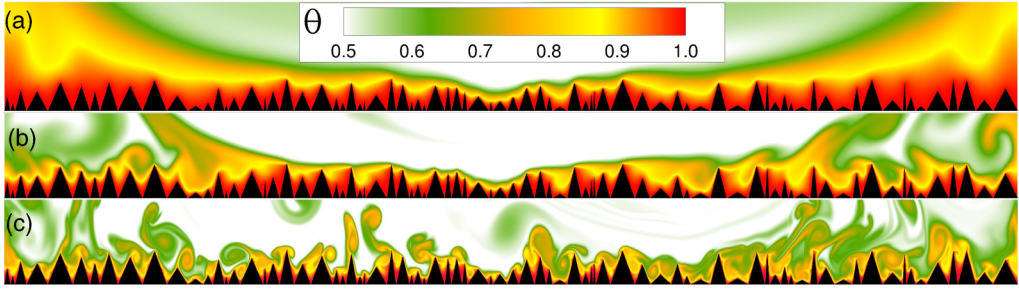
FIG. 11. Instantaneous temperature field near the bottom rough surface at (a) Ra $= 10^7$, (b) Ra $= 2.15 \times 10^8$, and (c) Ra $= 4.64 \times 10^9$ for R_1 roughness. Before the critical Ra$_c = 2.15 \times 10^8$, very few plume-emitting peaks appear, whereas a significantly large number of such peaks are evident beyond Ra$_c$

observed, as shown in Fig. 10(g). However, with increasing Ra, the strength and size of the corner rolls increase and become significant to wash out the cavities near the lateral walls. This feature becomes more pronounced at the highest Ra as shown in Fig. 10(i), which indicates that the corner rolls near the left-lateral wall coalesce to form a slender structure and compress the primary rolls. These diminished structures efficiently wash out the cavities owing to their higher tendency to enter the cavity regions.

For the smallest roughness (R_1) configuration, similar to the R_2 case, a double-roll state persists for the entire regime as shown in Figs. 10(j)–10(l), although the corner rolls do not grow with Ra anymore. A closer look near the bottom surface, shown in Fig. 11, reveals that insufficient plume-emitting active peaks at lower Ra allow the induced horizontal shear flow to create a smooth boundary layer over the rough surfaces. However, as Ra increases, the thermal boundary layer becomes thinner and hence exposes more peaks to the bulk fluid. Beyond the critical Ra$_c$, a sufficient number of peaks become active and the boundary layer is perturbed throughout the surface. Thermal plumes emitted from these peaks enter the bulk directly to enhance the so-called bulk-plume interaction, which further increases the heat flux and Nu(Ra) scaling exponent. A note on the variation of this exponent with the roughness configurations is relevant here. The secondary vortices are either weak or absent in the R_1 configuration due to too many roughness elements creating smaller throat regions. On the other hand, in the other two configurations (R_2 and R_3), the wider throat region causes strong secondary vortices, which is consistent with the previous study [26]. This feature is also reflected by the thermal boundary layer (TBL) thickness shown in some of the selected frames ($\geqslant$Ra$_c$) of Fig. 10. Note that the TBL is calculated using the well-known rms technique and defined as the vertical distance from the surface to the location of maximum temperature variance [1]. It is evident that the TBL does not follow the roughness texture and remains above it at Ra$_c$. However, it nearly covers the entire rough surface in R_2 and R_3 at Ra $= 4.64 \times 10^9$, indicating the washing out of the cavities. Since the increased turbulence in the cavities reduces the perturbation of the boundary layer, a drop in the scaling exponent becomes obvious as it behaves similarly to the smooth case in the cavities. These arguments agree well with the previous studies [35], where the wider throat region was found to strengthen the secondary vortices and reduce the Nu(Ra) scaling exponent. Therefore, the present study suggests that, in reality, both the height and width of randomly oriented roughness texture are responsible for the Nu(Ra) scaling.

In support of the above arguments, we detect the perturbation of thermal boundary layers with the help of a time-averaged temperature field in the vicinity of bottom rough surfaces. As shown in Fig. 12, the large temperature gradient is confined to a thin layer near the roughness elements and covers the entire surface in R_3, except for the places where the elements are closely packed. Qualitatively, this smooth covering of the surface shows the absence of the perturbed boundary layers. Also, the presence of the bulk-mean temperature is apparent at most of the surface in this
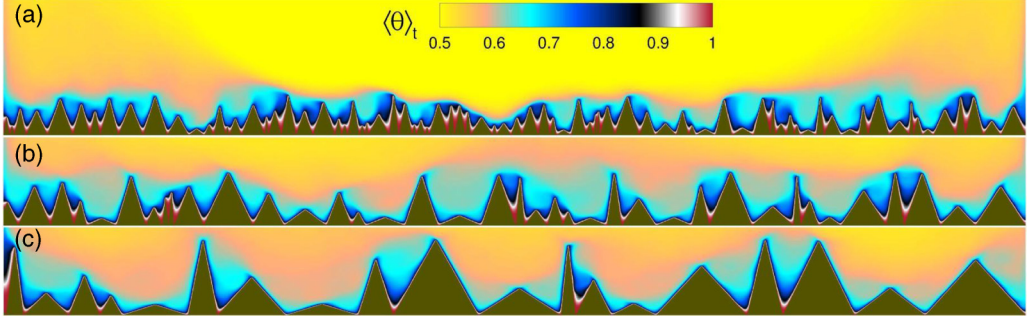
FIG. 12. Time-averaged temperature field close to the bottom plate for (a) R_1, (b) R_2, and (c) R_3 configurations for the highest $Ra = 4.64 \times 10^9$. The approach of the bulk-mean temperature increases with the overall heights of the roughness elements. A thin covering of the isothermal layer on the roughness elements at R_1 disappears, making it more prone to greater boundary layer perturbations

configuration. On the other hand, the boundary layer is highly disturbed in the R_1 configuration. In the latter, the bulk-mean temperature of the flow hardly approaches the cavity fluid. Clearly, a narrow spacing between the roughness elements in the R_1 case resists the bulk-mean temperature to reach the cavities and thus supports the boundary layer perturbation. On the other hand, a wider spacing helps in a thorough mixing of the cavity fluid that allows the bulk-mean temperature to approach the cavities, as seen in the R_3 case. These results support the above arguments related to the high turbulent intensity, which modifies the scaling exponent in the three configurations. Using a schematic diagram, Zhu *et al.* [20] showed the boundary layer perturbation near the rough surface, which is found to be qualitatively consistent with the present data. However, the disordered boundary layer nearly vanishes for the R_3 case [see Fig. 12(c)]. The present study shows that spacing between the roughness elements controls the boundary layer perturbation. Also, the geometric characteristics of random roughness reveal a complex interaction between the bulk-mean and near-wall temperatures, which was absent in the previous studies.

The above proposition qualitatively indicates that the heat flux enhancement mainly takes place due to the intense plume emission in the vicinity of the crest of the rough surfaces. To advance it we attempt to present a mechanism that induces the plume emission using the turbulent kinetic energy (TKE) budget close to the rough bottom surface. The TKE budget is written as

$$
\underbrace{\partial_t \left(\frac{1}{2} \overline{u_i' u_i'} \right) + U_j \partial_j \left(\frac{1}{2} \overline{u_i' u_i'} \right)}_{A} = \underbrace{- \overline{u_i' u_j'} S_{ij}}_{P_s} + \underbrace{g\beta \overline{u_i' \theta'} \delta_i y}_{P_b}
$$
$$
\underbrace{- 2\nu \overline{s_{ij}' s_{ij}'}}_{\epsilon} \underbrace{- \partial_j \left(\frac{1}{\rho} \overline{u_j' p'} + \frac{1}{2} \overline{u_i' u_i' u_j'} - 2\nu \overline{u_i' s_{ij}'} \right)}_{T},
$$

(9)

where the prime, overbar, s_{ij}, and S_{ij} represent the fluctuation, time-averaging, fluctuating, and mean strain rates, respectively. Note that the term on the left-hand side is advection A, while the terms on the right-hand side, in order of appearance, are shear production P_s, buoyancy production P_b, dissipation ϵ, and transport T, respectively [22,36]. In particular, we focus on the horizontal variation of the two production terms at four different Ra. In order to identify the contribution of the production terms, we show axial variation of P_b and P_s for $Ra_L = 3 \times 10^6$, which is below the critical threshold (Ra_c), and $Ra_I = 4.64 \times 10^8$ and $Ra_H = 4.64 \times 10^9$ above it, in addition to Ra_c. While buoyancy production signifies production of turbulent fluctuations by thermal plumes, shear production indicates the energy interaction between mean flow and turbulent fluctuations. As shown in Figs. 13 and 14, we present the variation of P_b and P_s in the horizontal direction just above the
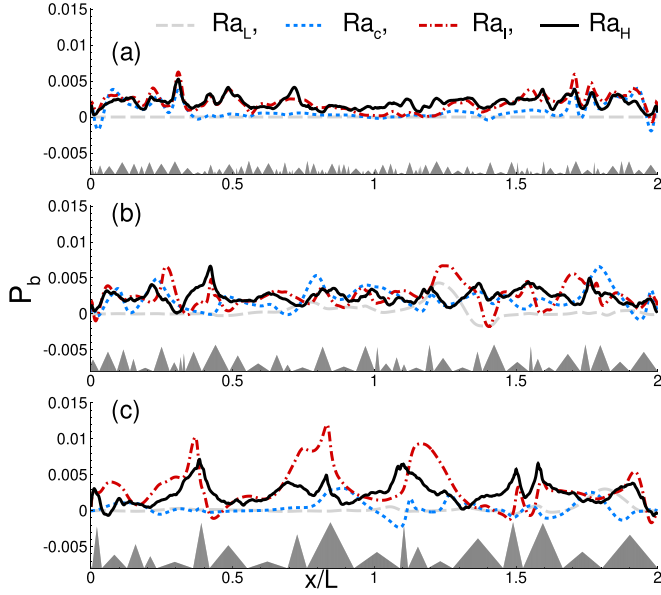
FIG. 13. Buoyancy production in (a) R_1, (b) R_2, and (c) R_3 before, at, and above the critical Rayleigh number Ra_c. Here Ra_L ($Ra = 3 \times 10^6$) indicates the Ra case lesser than Ra_c, while Ra_I and Ra_H show the intermediate- (4.64×10^8) and highest-Rayleigh-number cases (4.64×10^9), respectively.

tallest roughness element ($H/100$ unit). It is evident that below the critical Ra, the magnitude of the two components of TKE production is insignificant. However, as Ra increases, their magnitude and variation in the horizontal direction differ. Since P_b quantifies the strength of plumes, a sudden
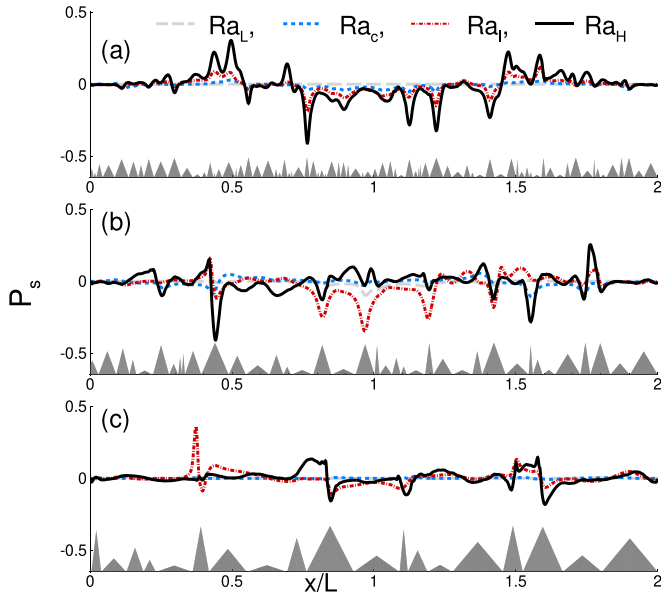

FIG. 14. Shear production in (a) R_1, (b) R_2, and (c) R_3 before, at, and after the critical Rayleigh number Ra_c. The labels are the same as in Fig. 13.

rise in peaks confirms the idea of activation of numerous peaks beyond the critical Ra. A similar observation is quite apparent in the R_2 and R_3 cases. We observe that the magnitude of buoyancy production is higher in the two taller configurations, which is quantified by peak values of P_b and their horizontal average. While the peak values at Ra_l are 0.0062, 0.0070, and 0.012 in the R_1, R_2, and R_3 configurations, respectively, their mean values (in the same order) for the highest simulated Ra (4.64×10^9) case are 0.001 98, 0.002 41, and 0.002 42. This happens due to frequent washing out of the cavities by the smaller rolls present in two taller roughness cases and direct emission of thermal plumes into the bulk. The transformation of large-scale rolls into smaller ones provides them with greater access to the cavities, which further supports why R_3 results in higher heat flux than the other configurations.

In terms of magnitude, shear production shows the opposite trend to P_b. In the R_1 case, P_s is significantly higher than R_2 and R_3. Note that higher P_s indicates transfer of energy from the mean flow to turbulent fluctuations. It is observed that a double-roll state remains stable in the R_1 case, which favors a strong lateral movement of fluid. The interaction between the mean flow and surface roughness increases with Ra, resulting in stronger velocity fluctuations. However, it seems obvious that multiple large-scale rolls hinder their motion, resulting in a flow that supports the vertical movement of thermal plumes more than the horizontal one. Thus, the two components of TKE production ascertain the significance of active peaks and reveals the strongly induced horizontal movement of fluid in the R_1 case.

C. Effect of roughness on flow strength

In the preceding section, we observed transformation of a double-roll state to a multiple-roll state in the R_2 and R_3 configurations, whereas the former remained unaltered throughout the simulated Ra range for the R_1 case. Here we study how stability of the DRS and its transformation impact the flow strength, which plays a crucial role in heat transport. In a previous investigation, Zhang *et al.* [37] quantified the strength of convection in terms of Reynolds number Re as

$$\mathrm{Re} = \frac{UH}{\nu}, \tag{10}$$

where $U = \sqrt{\langle \mathbf{u} \cdot \mathbf{u} \rangle_{V,t}}$. They observed Re $\sim$ Ra$^{0.59 \pm 0.02}$, which shows that the flow strength in a 2D geometry is stronger than its 3D (Re $\sim$ Ra$^{0.5}$) counterpart due to the absence of a lateral dimension which restricts the movement of plumes to escape in the third direction [38–40]. Consequently, the emitted thermal plumes drive the large-scale rolls and the corner rolls. Wang *et al.* [25] also used the same expression to quantify the strength of convection.

Figure 15(a) shows the variation of Re, normalized by the smooth case data (Re$_0$), with thermal forcing. Evidently, the flow strength in the smooth convection cell is significantly greater than that in the roughness cases in the lower-Ra range. Also, Re/Re$_0$ is the highest in R_1 and the least in R_3, showing a consistent decreasing trend with increasing roughness height in the simulated Ra range. The lower flow strength in taller roughness cases indicates that multiple rolls hinder the flow strength. In the lower-Ra range, a slight improvement in Re signifies the mobility of entrapped fluid. As Ra increases, roughness elements interrupt the flow, which results in a drop in Re/Re$_0$ in the Ra range (3×10^6)–(3×10^7). Subsequently, a further increase in thermal forcing yields a monotonically increasing trend in Re(Ra)/Re$_0$. Interestingly, Re in the R_1 case becomes comparable to the smooth case, Re/Re$_0 \approx 1$, in the enhanced heat flux regime. Eventually, it becomes greater than its smooth counterpart at the highest Ra. On the other hand, Re/Re$_0 < 1$ in the other two taller configurations indicates the reduced flow strength.

By recalling the enhanced heat flux due to roughness elements, we observe the contrasting role of roughness in impacting the flow strength. This contrasting behavior can be explained from the viewpoint of large-scale rolls. While multiple-roll states (MRSs) in R_2 and R_3 wash out the cavities efficiently, they impede the movement of flow. In other words, the taller roughness elements which directly emit thermal plumes in the bulk region also act as an obstacle for the large-scale rolls.
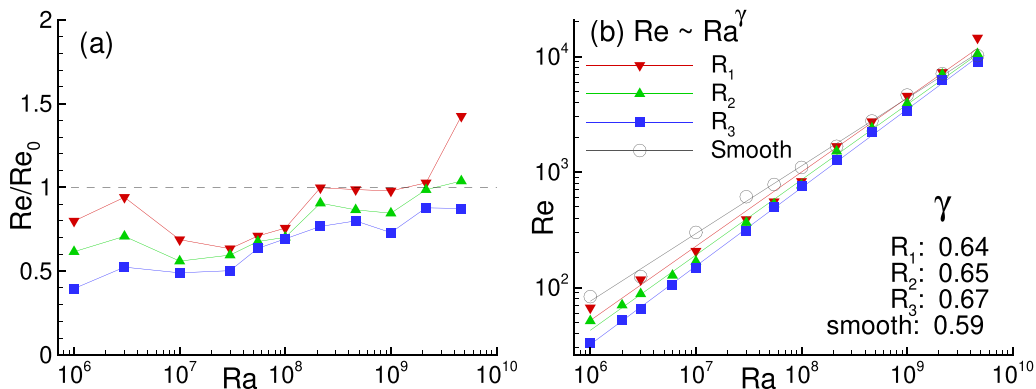
FIG. 15. (a) Variation of normalized Reynolds number Re/Re_0 with Ra for the three roughness cases. Note that Re_0 represents the Reynolds number for the smooth case. (b) The $Re \sim Ra^\gamma$ scaling law shows marginal improvement in γ for roughness cases

In contrast, the smallest roughness case exhibits appreciable improvement in Re. In the enhanced heat flux regime in the R_1 case, the tiny roughness elements become active and directly emit the thermal plumes in the bulk region, while below Ra_c, the contribution of these peaks in thermal plume emission is insignificant. Note that these active peaks impart a shearing effect on the large-scale rolls, which enhances the flow strength. This effect is seen in Fig. 14, where shear production in R_1 is significantly higher as compared to its taller roughness counterparts.

We further show the $Re \sim Ra^\gamma$ dependence for the three roughness configurations and smooth case in Fig. 15(b). For the smooth case, it is observed that $Re \sim Ra^{0.59}$, which is the same as reported by Zhang *et al.* [37]. However, the exponent is slightly higher in the roughness cases, although it is nearly equal for all of them, given by 0.64, 0.65, and 0.67 for R_1, R_2, and R_3, respectively. Note that only a slight improvement in γ indicates the insignificant impact of roughness elements on the Re(Ra) scaling law. This analysis clearly shows that altering the flow structures can enhance the heat flux without improving the flow strength. Larger roughness has greater tendency to alter the stable DRS of the low-Ra range as compared to the smaller elements.

D. Multilayer flow characteristics

The mean temperature profile in the vertical direction usually identifies two regions in the flow. Nearly half of the total temperature drop occurs near the plate, which results in Nu as the inverse of the thermal boundary layer thickness λ_θ, $Nu \approx 1/2\lambda_\theta$. Once the major temperature drop takes place near the plates, flow assumes a near homogeneous state in the central region, termed the bulk. It is expected that the mean temperature profile also reflects the characteristics of local flow structures. It is calculated by area-time averaging of the temperature field represented by $\langle\theta\rangle_{A,t}$, where A and t stand for area and time, respectively. In general, these profiles identify the well-mixed homogeneous bulk region. However, in a roughness-facilitated thermal convection, Zhu *et al.* [18] observed the effect of Ra on these profiles and proposed that the profiles become similar to that in the smooth case at higher Ra, which they argued as one indication of saturation of the enhanced exponent regime to the classical one.

Figure 16 shows the vertical profiles of mean temperature in the smooth, R_1, R_2, and R_3 cases to compare the impact of roughness on the bulk and near-wall region. At lower Ra, the mean temperature profiles in all the roughness cases show a smaller vertical extent of the homogeneous region. This indicates that bulk flow is more sensitive to roughness for weak thermal forcing. However, the vertical extent of the homogeneous region increases with Ra. A thicker thermal boundary layer at lower Ra extends the impact of roughness (see Fig. 16). The inset shows the
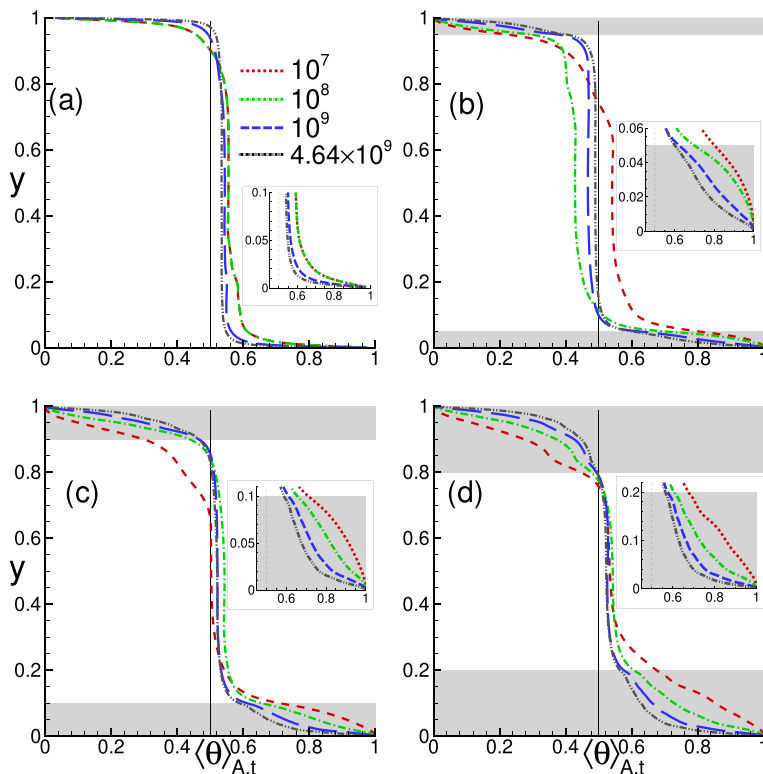
FIG. 16. Vertical area time-averaged temperature profiles in the (a) smooth, (b) R_1, (c) R_2, and (d) R_3 cases. The effect of Ra, ranging from 10^7 to 4.64×10^9, on flow characteristics is shown. The inset shows the vertical profiles inside the cavity region

vertical profiles close to the rough surface, where the temperature profiles vary with roughness configurations to show the distinct flow characteristics. The temperature falls slowly in the R_1 case as compared to the other configurations. Based on the temperature drop from the rough surface to the bulk, the flow is perceived to be composed of three layers. In the first layer (closest to the wall), the flow remains nearly stagnant and a sharp decrease in temperature due to thermal resistance in the valleys is observed. The second or intermediate layer shows a nonlinear drop in temperature with a smaller temperature gradient. It is expected that this layer is controlled by secondary vortices present inside the cavities. The third layer represents the bulk flow, where large-scale rolls control the flow. Since strong secondary vortices and a transition from the DRS to the MRS occur in the R_3 configuration, the second layer seems more prominent in this roughness setup [see Fig. 16(d)].

As shown in Fig. 17, the temperature drop in three layers is ascertained by calculating the absolute magnitude of the temperature gradient ϕ_θ as

$$\phi_\theta = \left| \frac{d \langle \theta \rangle_{A,t}}{dy} \right|. \tag{11}$$

In the smooth case, the slope is maximum at the surface while it increases with y in the roughened configuration to attain a maximum before dropping asymptotically to the bulk-mean value. This dual characteristic of the temperature gradient confirms the multilayer flow behavior. At a smaller Ra a peak in ϕ_θ is seen to occur at a distance ($y \approx H/20$) for the R_1 case owing to the lack of ventilation in the narrowly packed throats. However, with the increase in thermal forcing the temperature gradient shifts mainly to the vicinity of the rough surface. A nearly trivial profile of ϕ_θ for $y > H/40$ in
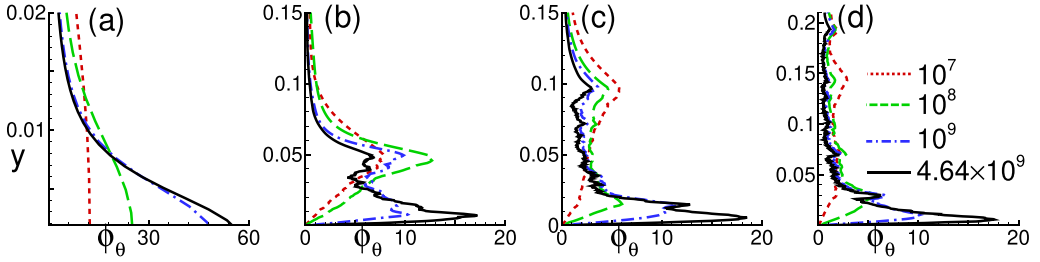
FIG. 17. Vertical profile of the absolute temperature gradient calculated as $|d\langle\theta\rangle_{A,t}/dy|$ in the (a) smooth, (b) R_1, (c) R_2, and (d) R_3 cases

R_2 and R_3 clearly indicates mixing of the fluid and the lesser extent of an entrapped plume at all Ra. Interestingly, the first layer is evident in all three configurations and appears to be independent of the nature of rough surfaces. The profiles of mean temperature are further normalized by the vertical distance at which ϕ_θ attains an absolute maximum in the highest-Ra case. Figure 18 clearly identifies the above-mentioned three layers. The inset shows the enlarged view where the three profiles nearly collapse onto each other in the first layer, which is weakly nonlinear in nature. This signifies a marginal drop in temperature with a sudden increase in vertical height, which indicates a region of stagnant fluid where heat is transported mainly through conduction. Note that, despite a huge difference in the roughness scales present in the three configurations, a characteristic of the first layer is independent of roughness geometry. Flow behavior in the second or intermediate layer is controlled by secondary vortices, which mimic the bulk flow and suddenly change its behavior beyond the maximum roughness height, i.e., in the third layer. In the R_3 case, the mean temperature profile in the intermediate layer continues to drop roughly in the same manner as it does in the third layer. The strong influence of secondary vortices improves the bulk-cavity flow interaction, which results in effective thermal convection inside the cavities. Such an effect of secondary vortices that enhance the heat flux by improving the mixing inside the cavities was also reported by Zhang *et al.* [19] for monoscale triangular roughness in a 2D convection cell. In the bulk-flow-controlled layer (third layer), the fluid temperature remains the same irrespective of the nature of the rough surface.
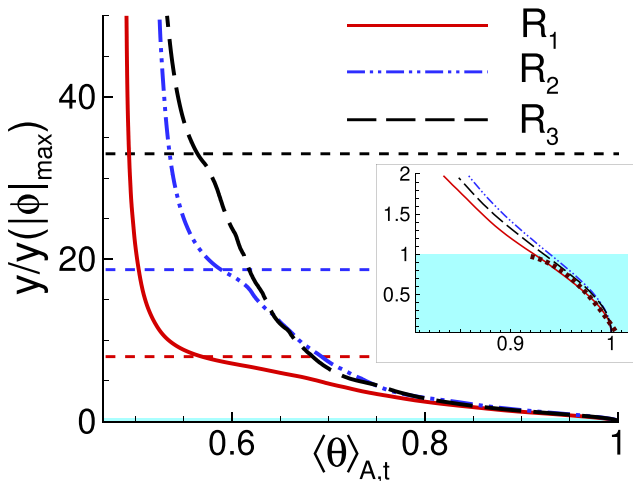

FIG. 18. Vertical variation of the mean temperature profile with $y/y(|\phi_\theta|_{\max})$, where $|\phi_\theta|_{\max}$ is the location where ϕ_θ becomes maximum, for the highest Ra (4.64×10^9). The inset shows a close-up view of the first layer where all three profiles exhibit a weakly nonlinear behavior

Based on the vertical profiles of the mean temperature in three levels of random roughness, we propose that the second layer plays a crucial role in enhancing the heat flux. The greater its resemblance to the bulk, higher the heat flux, as it is in R_3. It also supports the prospect of washing out the cavities. Strong secondary vortices sweep the cavities appropriately to detach the thermal boundary layer, which was attached to the rough surfaces.

IV. SUMMARY AND CONCLUSIONS

The present work has explored the effect of rough boundaries on both heat transport and flow dynamics in two-dimensional turbulent RBC. Though roughness elements of varying height and base are present, the onset of the enhanced heat flux regime, with different Nu(Ra) scaling exponents, is triggered at different critical thermal forcing depending on the maximum roughness height. Such an onset is marked by a transformation from a double to a single peak in the PDF of temperature fluctuations in the bulk and discontinuities in the near-wall contribution of the thermal dissipation rate. Unlike the smooth case, near-wall and global estimates of ϵ_θ become invariant to Ra in the enhanced heat flux regime. However, below the critical Ra, the $\epsilon - \mathrm{Ra}$ dependence shows evidence of the classical scaling. Thus, an increase in the Nu(Ra) scaling with a near-constant near-wall contribution to thermal dissipation suggests a mixed view of the effect of the boundary layer at high Ra.

The bulk-plume interaction, which is seen to facilitate an enhanced scaling for all roughness heights, is achieved through different routes. For the tallest roughness heights, large-scale rolls break down into smaller ones which can enter the cavities more efficiently and sweep the boundary layer. These smaller rolls enhance the mixing of fluid in the cavity regions to emit intense thermal plumes more frequently. However, the growing strength and size of the corner rolls, at intermediate roughness heights, evacuate the cavities near the lateral walls and reduce the size of the primary rolls. On the other hand, owing to their ability to penetrate the boundary layer faster, a smaller roughness setup creates more plume-emitting active spots. Thus, not only the tilt of the cell but also rough surfaces induce complex roll states or distorted structures which result in increased heat flux. Variation in buoyancy production just above the roughness peaks in the smallest roughness case confirms the idea of activation of plume-emitting peaks. Moreover, the highest buoyancy production of turbulent kinetic energy in the tallest roughness case confirms the enhanced heat flux. However, the opposite trend in shear production indicates greater lateral movement for the smallest roughness setup.

It was further found that random roughness plays an intricate role in influencing the two global transport properties Re and Nu. In contrast to its effect on heat flux, the flow strength (Re) drops in the two taller roughness configurations and improves for the smallest roughness case at Ra = 4.64×10^9. A decrease in Re is attributed to the presence of a multiple-roll state which hinders the motion of large-scale rolls. Also, an insignificant change is observed in the Re(Ra) scaling exponents showing a weak effect of roughness on flow strength. The vertical mean temperature profile near the rough surface shows evidence of multilayer flow characteristics. A weakly nonlinear profile closest to the wall exhibits collapse of data for all the roughness setups. We proposed that the intermediate layer plays a crucial role in heat transfer enhancement. The greater its resemblance to the bulk, the higher the heat flux. Beyond the maximum roughness height the flow asymptotically approaches the bulk through the outer layer.

[1] G. Ahlers, S. Grossmann, and D. Lohse, Heat transfer and large scale dynamics in turbulent Rayleigh-Bénard convection, Rev. Mod. Phys. **81**, 503 (2009).

[2] F. Chilla and J. Schumacher, New perspectives in turbulent Rayleigh-Bénard convection, Eur. Phys. J. E **35**, 58 (2012).

[3] B. Castaing, G. Gunaratne, F. Heslot, L. Kadanoff, A. Libchaber, S. Thomae, X. Wu, and S. Zanetti, Scaling of hard thermal turbulence in Rayleigh-Bénard convection, J. Fluid Mech. **204**, 1 (1989).

[4] B. I. Shraiman and E. D. Siggia, Heat transport in high-Rayleigh-number convection, Phys. Rev. A **42**, 3650 (1990).

[5] W. V. R. Malkus, The heat transport and spectrum of thermal turbulence, Proc. R. Soc. London **225**, 196 (1954).

[6] R. H. Kraichnan and S. Chandrasekhar, Turbulent thermal convection at arbitrary Prandtl number, Phys. Fluids **5**, 1374 (1962).

[7] S. Grossmann and D. Lohse, Scaling in thermal convection: A unifing theory, J. Fluid Mech. **407**, 27 (2000).

[8] S. Grossmann and D. Lohse, Thermal Convection for Large Prandtl Numbers, Phys. Rev. Lett. **86**, 3316 (2001).

[9] S. Grossmann and D. Lohse, Fluctuations in turbulent Rayleigh-Bénard convection: The role of plumes, Phys. Fluids **16**, 4462 (2004).

[10] M. J. Tummers and M. Steunebrink, Effect of surface roughness on heat transfer in Rayleigh-Bénard convection, Int. J. Heat Mass Transf. **139**, 1056 (2019).

[11] Y.-B. Du and P. Tong, Turbulent thermal convection in a cell with ordered rough boundaries, J. Fluid Mech. **407**, 57 (2000).

[12] S. Toppaladoddi, A. J. Wells, C. R. Doering, and J. S. Wettlaufer, Thermal convection over fractal surfaces, J. Fluid Mech. **907**, A12 (2021).

[13] M. Belkadi, L. Guislain, A. Sergent, B. Podvin, F. Chillà, and J. Salort, Experimental and numerical shadowgraph in turbulent Rayleigh-Bénard convection with a rough boundary: Investigation of plumes, J. Fluid Mech. **895**, A7 (2020).

[14] Y. Shen, P. Tong, and K.-Q. Xia, Turbulent Convection over Rough Surfaces, Phys. Rev. Lett. **76**, 908 (1996).

[15] S. Ciliberto and C. Laroche, Random Roughness of Boundary Increases the Turbulent Convection Scaling Exponent, Phys. Rev. Lett. **82**, 3998 (1999).

[16] P.-E. Roche, B. Castaing, B. Chabaud, and B. Hébral, Observation of the $\frac{1}{2}$ power law in Rayleigh-Bénard convection, Phys. Rev. E **63**, 045303(R) (2001).

[17] S. Toppaladoddi, S. Succi, and J. S. Wettlaufer, Roughness as a Route to the Ultimate Regime of Thermal Convection, Phys. Rev. Lett. **118**, 074503 (2017).

[18] X. Zhu, R. J. A. M. Stevens, R. Verzicco, and D. Lohse, Roughness Facilitated Local 1/2 Scaling Does Not Imply the Onset of the Ultimate Regime of Thermal Convection, Phys. Rev. Lett. **119**, 154501 (2017).

[19] Y. Zhang, C. Sun, Y. Bao, and Q. Zhou, How surface roughness reduces heat transport for small roughness heights in turbulent Rayleigh-Bénard convection, J. Fluid Mech. **836**, R2 (2018).

[20] X. Zhu, R. J. A. M. Stevens, O. Shishkina, R. Verzicco, and D. Lohse, $Nu \sim Ra^{1/2}$ scaling enabled by multiscale wall roughness in Rayleigh-Bénard turbulence, J. Fluid Mech. **869**, R4 (2019).

[21] D.-L. Dong, B.-F. Wang, Y.-H. Dong, Y.-X. Huang, N. Jiang, Y.-L. Liu, Z.-M. Lu, X. Qiu, Z.-Q. Tang, and Q. Zhou, Influence of spatial arrangements of roughness elements on turbulent rayleigh-bénard convection, Phys. Fluids **32**, 045114 (2020).

[22] K. Chand, M. Sharma, V. T. Vishnu, and A. K. De, Statistics of coherent structures in two-dimensional turbulent Rayleigh-Bénard convection, Phys. Fluids **31**, 115112 (2019).

[23] M. S. Emran and O. Shishkina, Natural convection in cylindrical containers with isothermal ring-shaped obstacles, J. Fluid Mech. **882**, A3 (2020).

[24] Q. Wang, Z.-H. Wan, R. Yan, and D.-J. Sun, Flow organization and heat transfer in two-dimensional tilted convection with aspect ratio 0.5, Phys. Fluids **31**, 025102 (2019).

[25] Q. Wang, R. Verzicco, D. Lohse, and O. Shishkina, Multiple States in Turbulent Large-Aspect-Ratio Thermal Convection: What Determines the Number of Convection Rolls?, Phys. Rev. Lett. **125**, 074501 (2020).

[26] K. Chand, M. Sharma, and A. K. De, Significance of near-wall dynamics in enhancement of heat flux for roughness aided turbulent Rayleigh-Bénard convection, Phys. Fluids **33**, 065114 (2021).

[27] R. Verzicco and R. Camussi, Prandtl number effects in convective turbulence, J. Fluid Mech. **383**, 55 (1999).

[28] A. K. De, A diffuse interface immersed boundary method for complex moving boundary problems, J. Comput. Phys. **366**, 226 (2018).

[29] A. De, A diffuse interface immersed boundary method for convective heat and fluid flow, Int. J. Heat Mass Transf. **92**, 957 (2016).

[30] O. Shishkina, R. J. A. M. Stevens, S. Grossmann, and D. Lohse, Boundary layer structure in turbulent thermal convection and its consequences for the required numerical resolution, New J. Phys. **12**, 075022 (2010).

[31] Y.-C. Xie and K.-Q. Xia, Turbulent thermal convection over rough plates with varying roughness geometries, J. Fluid Mech. **825**, 573 (2017).

[32] M. Sano, X. Z. Wu, and A. Libchaber, Turbulence in helium gas free convection, Phys. Rev. A **40**, 6421 (1989).

[33] J. Salort, O. Liot, E. Rusaouen, F. Seychelles, J.-C. Tisserand, M. Creyssels, B. Castaing, and F. Chillà, Thermal boundary layer near roughnesses in turbulent Rayleigh-Bénard convection: Flow structure and multistability, Phys. Fluids **26**, 015112 (2014).

[34] G. Stringano, G. Pascazio, and R. Verzicco, Turbulent thermal convection over grooved plates, J. Fluid Mech. **557**, 307 (2006).

[35] S. Wagner and O. Shishkina, Heat flux enhancement by regular surface roughness in turbulent thermal convection, J. Fluid Mech. **763**, 109 (2015).

[36] K. Petschel, S. Stellmach, M. Wilczek, J. Lülff, and U. Hansen, Kinetic energy transport in Rayleigh-Bénard convection, J. Fluid Mech. **773**, 395 (2015).

[37] Y. Zhang, Q. Zhou, and C. Sun, Statistics of kinetic and thermal energy dissipation rates in two-dimensional turbulent Rayleigh-Bénard convection, J. Fluid Mech. **814**, 165 (2017).

[38] J. J. Niemela, L. Skrbek, K. R. Sreenivasan, and R. J. Donnelly, The wind in confined thermal convection, J. Fluid Mech. **449**, 169 (2001).

[39] X.-L. Qiu and P. Tong, Large-scale velocity structures in turbulent thermal convection, Phys. Rev. E **64**, 036304 (2001).

[40] E. Brown, D. Funfschilling, and G. Ahlers, Anomalous Reynolds-number scaling in turbulent Rayleigh-Bénard convection, J. Stat. Mech. (2007) P10005.